AIAA JOURNAL
Vol. 38, No. 9, September 2000

Optical Alignment Tolerances and Techniques for Particle Image Velocimetry

T. Drouillard, P. McCarthy,* and M. Linne†
Colorado School of Mines, Golden, Colorado 80401

To ensure good particle image velocimetry correlations, it is necessary to characterize the important variables that control image acquisition and image analysis. Among these, image spot size as it changes across the entire imaging surface bears investigation. Therefore, we describe an error analysis for subpixel resolution of correlation peaks using Whittaker's method. These results set a tolerance on optimum image spot sizes. Typical lenses are then analyzed using ray-trace software, to ascertain what optical parameters and camera misalignments are allowable within these optimum tolerances. We then describe an alignment procedure that allows us to set a camera to those tolerances.

Introduction

TO acquire high-quality particle image velocimetry (PIV) data, it is necessary to use a cross-correlation technique, for example, two-color or image-shifted PIV, to align carefully the optical system and use an optimized data analysis package. In recent work performed at the Colorado School of Mines (CSM), two PIV investigations resulted in 1) an assessment of the effects of particle image spot size on correlation accuracy, 2) determination of the minimum spot size for least error, and 3) the development of an experimental system that can reliably generate this minimum spot size.

One of these projects involved the development of PIV analysis software that generates vector data from PIV images (Ref. 1; T. Drouillard and M. Linne, "Experiments in Fluids," manuscript in preparation). In that work, several techniques for resolving correlation peaks were evaluated. These included the basic centroid method, Whittaker's reconstruction, an analytical three-point Gaussian fit, and a numerical five-point Gaussian fit using the Marquardt method. An assessment of reconstruction errors was included. The least error was produced by the five-point Gaussian fit using Marquardt nonlinear fitting, whereas Whittaker's reconstruction was a close second. Furthermore, it was found that the size of the correlation peak (directly related to particle image spot size) has the greatest effect on the accuracy of the reconstruction algorithm. This sets a tolerance on the image spot size. That work is discussed in detail by Drouillard and Linne (manuscript in preparation).

A second project involved the development of a method by which a PIV experimental apparatus may be consistently and reproducibly aligned to meet this tolerance on spot size.[2] This topic is of primary importance to chemical film-based techniques, where turnaround time is very long. It also has implications for digital systems, especially when it is necessary to align a camera across a large system, from within a wind tunnel, for example. A portion of this investigation included modeling photographic lens performance under ideal and nonideal conditions using computer-based geometric ray tracing. These results provide insight into how various experimental configurations can lead to spot size variation, which in turn affects the accuracy of PIV analysis. Based on such results, a system for alignment of the experiment was developed. That work is the primary focus of this paper.

Maximum Allowable Spot Size for Minimum Error

Whittaker's Reconstruction

The primary PIV analysis step during which image spot size contributes significantly is at the point of correlation peak detection. Peak detection is the step in which an algorithm is applied to discrete (whole-pixel) correlation results, to calculate displacement vector components with subpixel precision. In a forthcoming paper (Drouillard and Linne, manuscript in preparation), Whittaker's method, the centroid method, and two different Gaussian fits for peak detection are compared. A numerical five-point Gaussian fit using Marquardt's nonlinear fitting routine is shown to provide the lowest uncertainty when the correlation result contains noise peaks (as it always will). Whittaker's reconstruction, although somewhat more uncertain, generates less uncertainty than the centroid method and an analytical three-point Gaussian fit. The Marquardt method is not currently used by PIV researchers, whereas Whittaker's reconstruction is used commonly for this task.[3] For the purposes of this paper, therefore, we discuss camera alignment in the context of the Whittaker results. This is an acceptable approach because both the Marquardt and Whittaker techniques generate the same spot size tolerance. In what follows, therefore, we briefly describe how the Whittaker technique can be used to generate an image spot size tolerance, following which we discuss how that tolerance can be met with standard imaging systems.

In this work, a correlation peak is emulated synthetically by a Gaussian function, because correlation peaks that are derived from diffraction-limited spots are best represented by a Gaussian.[3] A diffraction-limited spot pattern follows the Airy function,[4] but the convolution of two Airy functions is nearly Gaussian. As we demonstrate, the diffraction limit is not always achieved. This approach remains valid, however, because we wish to set a minimum spot size tolerance for PIV imaging, and at the minimum, the spot will be diffraction limited or nearly diffraction limited.

The synthetic peak (Gaussian function) is then sampled at discrete locations (on a per-pixel basis, as it would be with experimental data), and then Whittaker's reconstruction is used with the synthetic sample points to interpolate the location of the peak. The locations of the actual peak (from the original Gaussian function) and the interpolated peak are compared.

The form of the one-dimensional Gaussian function is given by

$$g(t) = \exp\left[-\frac{(t - t_0)^2}{w^2}\right] \tag{1}$$

In Eq. (1), t is location (in space here) and w controls the width of the distribution. The function is characterized by a peak magnitude of unity, a peak location t_0 occurring on the interval $2.5 \leq t \leq 3.5$ so that the maximum sample value occurs at $t = 3$, and a width w proportional to the full width at half-maximum (FWHM) value by

$$w = \frac{\text{FWHM}}{2\sqrt{\ell n 2}} \tag{2}$$

The Gaussian function is then sampled discretely at $t = 1$, 2, 3, 4, and 5, to emulate the pixilation process. Whittaker's reconstruction, shown in Eq. (3), is then used to reconstruct the continuous function

Received 10 April 1999; revision received 27 January 2000; accepted for publication 18 February 2000.

*Research Assistant, Center for Commercial Applications of Combustion in Space.
†Professor, Center for Commercial Applications of Combustion in Space; mlinne@mines.edu.

$$g'(t) = \sum_{t_n=1}^{5} g_{t_n} \operatorname{sinc}\left[\frac{\pi}{T_s}(t - t_n)\right] \quad (3)$$

In Eq. (3), $g'(t)$ is the approximate, reconstructed Gaussian, g_{t_n} is the sampled value at the sample point t_n, and T_s is the sampling interval. In short, sinc functions at each sample point are scaled by the magnitude of the sampled function at each of these points, and then added to reconstruct the complete interpolated function. Because samples are separated by an interval of one (representing whole pixels), the sampling interval T_s is 1.0. Following this, the location of the reconstructed peak is found.

The lowest error in peak recovery occurs when a sample point coincides with the actual peak of the sampled function. This is an uncommon occurrence. The first step, therefore, in determining how the imaging and sampling process affects the peak-location error was to vary the offset between the Gaussian peak and the sample points, for various values of width w. A clear relationship between this offset and error in peak location was found (see Fig. 1). It was also determined that there is an optimum Gaussian width, and that increasingly narrow and increasingly wide Gaussian functions both give increasingly erroneous reconstructions. Two graphs are shown in Fig. 1. The vertical axis contains relative error, whereas the horizontal axis contains offset between the Gaussian peak and the sample points (scale is in pixels). Figure 1a is a series of error plots for FWHM values of 2.6, 2.0, 1.4, 0.8, and 0.2. These are Gaussian functions that are increasingly narrow as the FWHM value decreases. Similarly, Fig. 1b is a series of error plots where the FWHM values increase, including the values 2.6, 3.2, 3.8, 4.4, and 5.0. In both graphs (Figs. 1a and 1b), as the width of the correlation peak decreases or increases away from the nominal value, the error of the interpolated peak location grows in magnitude. Also, the offset value at which maximum error occurs grows farther from the center sample value in both cases. Although similar in appearance, the cause is different for narrowing and widening peaks. As the Gaussian becomes more narrow, the center sample value remains large while

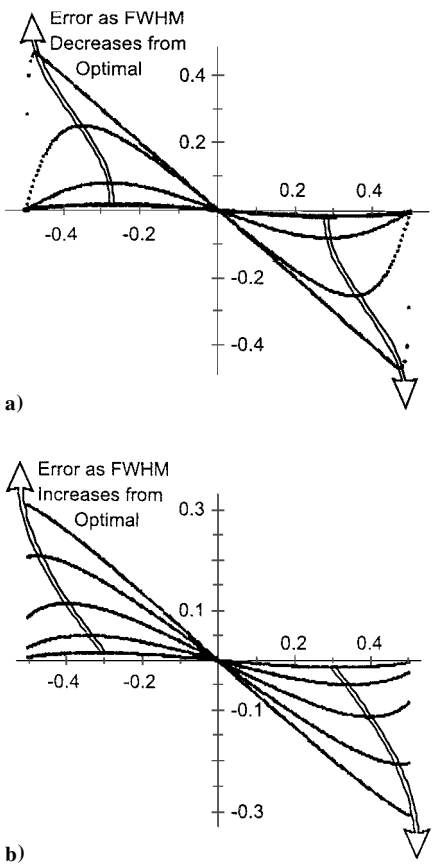

Fig. 1 Trend of increasing error with offset between sample points and the true Gaussian peak as width (FWHM) deviates from the optimal value.

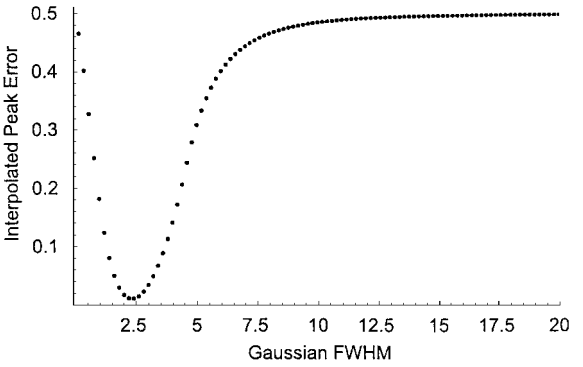

Fig. 2 Maximum error in peak location vs FWHM.

the adjacent sample values approach zero. It is difficult to reconstruct a function and its peak when there are few real data points one can use. In the extreme case, where sampled values approach zero at $t = 1$, 2, 4, and 5, the reconstructed peak is detected at the center sample point 3. In the case of an extremely wide Gaussian, the five sampled values are very close in magnitude, and all are significantly greater than zero. The reconstruction algorithm produces a function that passes through the sample values at $t = 1, 2, 3, 4$, and 5, and with a magnitude of zero at $t = \ldots, -2, -1, 0$ and at $t = 6, 7, 8, \ldots$. The reconstructed function approaches a top hat, the peak of which is located toward the center by Whittaker's method, as the sampled values become more equal.

Error was then calculated for Gaussian functions with FWHM values ranging from 0.2 to 20 in increments of 0.2, while varying the offset between the Gaussian peak and the sample points. The maximum error value for each FWHM were then plotted against the FWHM in Fig. 2. The peak offset values are, therefore, different from point to point in Fig. 2 because the offset that generates maximum error changes with FWHM, as shown in Fig. 1. Based on the results in Fig. 2, we conclude that a FWHM value of 2.4 is optimal for Whittaker's reconstruction. Ideal correlation peaks have a width of approximately five pixels (or sample points). The application of Whittaker's method to an excessively wide or excessively narrow correlation peak essentially results in inappropriate sampling of the peak, as already discussed.

This error constraint simply ensures that the correlation peak fits well within the area used for Whittaker reconstruction. We reach the same conclusion using the five-point Marquardt fit to a Gaussian, for the same basic reason. It is always possible to use more pixels, and then relax this requirement to make sure the correlation peak fits well within the larger collection of sample points. We chose 5 pixels here because this number ensures good peak resolution. This choice also comes fairly close to the imaging limitations of modern camera lenses (as described later), and so it ensures the largest spatial dynamic range while providing optimum images for peak detection.

The foregoing results are the outcome of a one-dimensional analysis. We have performed a similar analysis in two dimensions. A discussion of that work is contained in our companion paper (Drouillard and Linne, manuscript in preparation). Space limitations preclude a detailed discussion here, but we can state that errors in peak recovery for the two-dimensional problem are equal to the errors we find in the one-dimensional problem discussed. This outcome occurs because the two-dimensional error components are weakly nonlinear, nearly orthogonal manifestations of the one-dimensional uncertainty.

Correlation Width and Particle Image Size

To proceed with imaging analysis, it is necessary to relate the optimum width of the correlation peak found earlier to the particle image size at the camera imaging plane. The correlation of a Gaussian with itself is a somewhat wider Gaussian. It is straightforward to show that the width of the cross correlation will be $\sqrt{2}$ times the width of the original Gaussian particle image. The cross correlation of an Airy function is nearly Gaussian (the maximum error that occurs when fitting a Gaussian to a cross-correlated Airy function is roughly 1.5%). In this case, the width of the cross correlation will

be 1.3 times the width of the Airy function. The two values are quite close, but in this work we are investigating spot images that are not diffraction limited. Therefore, we take 1.4 as a conversion factor between correlation width and particle image size.

The relationship between pixel size and actual linear dimensions, for example, millimeters, is affected by the magnification of the optical system, and the pixel size in a charge-coupled device (CCD) or the resolution of the scanner used to digitize a chemical-film PIV image. A typical PIV image uses an interrogation cell size of 1 mm^2, which can be represented by a 64×64 array of pixels. This gives the relationship of 64 pixels/mm (or 16 μm per pixel) in relating experimental measurements to pixilated images. This pixel size represents the performance of our Nikon Coolscan film scanner. It is straightforward, however, to scale the results presented to other sizes using the numbers given here. Using these values, if the ideal correlation peak width as dictated by Whittaker's reconstruction is 2.4 pixels, a particle image size of approximately 1.7 pixels, or 27 μm, is desirable. We, therefore, set an image spot size tolerance at less than 30 μm.

Considerably more detail on errors in peak detection algorithms is provided by Drouillard and Linne (manuscript in preparation). Our goal here is to investigate the impact of these findings on the experiment itself. For this reason, we now discuss image spot sizes in real camera systems and how they can be controlled for minimum error.

Sources of Uncertainty in the Whittaker Models

The assessments of Whittaker's reconstruction were implemented in Mathematica.[5] The default numerical precision of values returned from Mathematica functions and algorithms is 16 digits. Intrinsic Mathematica functions that were used in this analysis include the exponential function (from which Gaussian curves and surfaces are constructed) and the sine function (used to calculate the sinc functions used in Whittaker's reconstruction). Sample points on which Whittaker's reconstruction is implemented and the reconstructed functions are, therefore, accurate to 16 digits as compared to the purely analytical forms that they represent.

To obtain the location of the peak in the respective curves or surfaces reconstructed by Whittaker's method, Mathematica's FindMinimum function[5] is implemented on the negative of the curve or surface. The FindMinimum routine employs the conjugate gradient method to locate a local minimum of a function of one independent variable and Powell's method for a surface function minimum. Both algorithms locate the minimum of a function through recursive processes, where repeated iterations increase accuracy, and are detailed in mathematical computing texts.[6] Mathematica completes a sufficient number of iterations to achieve 16-digit precision. Therefore, given the analytical form of a reconstructed function obtained by Whittaker's method, each of the location coordinates of the peak as described by Mathematica match the analytical peak location values within 16 digits.

Experimental Control of Spot Size

Diffraction Limit

Photographic lens performance and image resolution are fundamentally limited by diffraction. A point source of light mapped to an image plane with a diffraction-limited lens will produce an Airy irradiance distribution, which represents the smallest attainable spot size for any real optical imaging system.[4] The limit of image resolution can then be described using Rayleigh's criterion:

$$\Delta l_{\min} = 1.22\lambda(f\#) \tag{4}$$

where $\Delta l_{\min}$ is the minimum resolvable displacement between two Airy functions, λ is the optical wavelength, and $f\#$ is the lens f-number ($f\# \equiv$ focal length/aperture diameter). Rayleigh's criterion considers two point sources of light that are just discernable when the first irradiance ring of the primary Airy function overlaps the central irradiance peak (center) of the secondary Airy function (Fig. 3).

Extending this definition of image resolution to include magnification and expressing the size of the Airy function in terms of its diameter rather than its radius yields

$$d_s = 2.44(1 + M)\lambda(f\#) \tag{5}$$

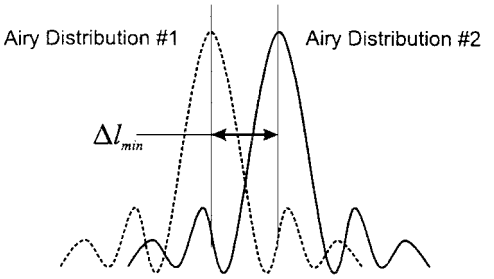

Fig. 3a Resolved airy patterns according to Rayleigh's criterion.

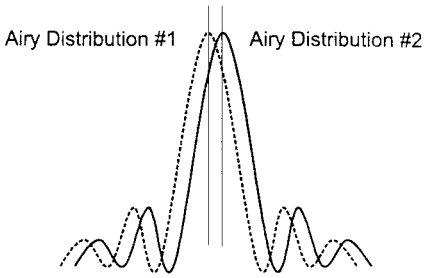

Fig. 3b Unresolved Airy patterns according to Rayleigh's criterion.

where M is the lens magnification. This form of the point response function was proposed by Adrian[7] and Keane and Adrian[8] as an estimation of the spot size, for use in their figures of merit.

Optical Aberrations and Imaging Systems

Expression (5) is certainly convienient, and it accurately describes the diffraction-limited performance of a lens. To reach the diffraction limit off-axis using normal lens apertures, however, is uncommon. Off-axis lens aberrations can limit the practical utility of a PIV image. We have, therefore, chosen to extend the imaging analysis by Adrian[7] and Keane and Adrian[8] to more complex situations. Unfortunately, to do this requires that we analyze specific lens designs, and this removes the appealing generality of Eq. (5). Here we have analyzed three common focal length lenses, to provide as much information as possible.

Geometrical optics (ray trace) is the most common technique for analyzing optical systems and for quantifying optical aberration.[4] The primary sources of optical aberration contributing to image distortion are longitudinal third-order spherical aberration (typically occurs when the paraxial approximation is not met), coma, and astigmatism (off-axis phenomena). These effects can be quantified easily via analysis if the optical prescription of the photographic lens used in the experimental diagnostic is known. Unfortunately, specific optical prescriptions for photographic lenses are generally not available from lens manufacturers. Therefore, we have analyzed lens prescriptions that are available, choosing the design that best reproduces the specifications of the two Nikon lenses that we use in the laboratory for small flowfields. Because PIV has been increasingly applied to wind tunnels, we have also analyzed a zoom lens that represents an approximation to current wind-tunnel practice.

In this analysis, a commercial ray-trace software package (Sigma 2100) was employed. This software allows lens parameters (compound lens combinations, lens spacing, optical materials, diameters and radii of curvature, adjustable aperture, and so forth) to be entered. The code then traces geometric rays for the specified optical system, generating image results that include optical aberrations (but do not include diffraction effects).

Three photographic lenses were selected for analysis. The first is a 100-mm lens with parameters specified in a commercially available optical database.[9] The second is a 55-mm lens specified in Ref. 10. These two lenses best represent the equipment we use in our laboratory for small flowfields (imaging 1:1). The third lens is a 200-mm zoom specified in the same commercial database as the 100-mm lens.[9] This lens applies to wind-tunnel work (imaging 10:1). These lens designs are somewhat inferior to currently available photographic lenses. One can then assume that a modern,

good-quality lens will match or outperform the lenses analyzed here. Our results, therefore, are a lower bound on lens performance.

For imaging applications, the physical dimensions of the film plane (24 × 35 mm for chemical film) ultimately define the field of view, as illustrated for the 1:1 case in Fig. 4. Object points located 12 and 17 mm from the origin describe the boundaries of the image plane. Therefore, in the spot diagram analysis to follow, both a 12- and a 17-mm field of view are considered.

Imaged particles are defined by coordinate points in the object plane. For reference, the origin of the optical axis z is located at the origin of the object plane. Locations in the object plane are defined in terms of x and y (horizontal and vertical). A point is placed in the object plane and then projected through the specified lens onto the image plane by the ray-trace software, while minimizing the optical path differences between respective rays, thus bringing the lens as near to focus as possible. Figure 5 shows a ray propagating from the point (x, y, $z = 0$, 12, 0), through the 55-mm lens to the image plane.

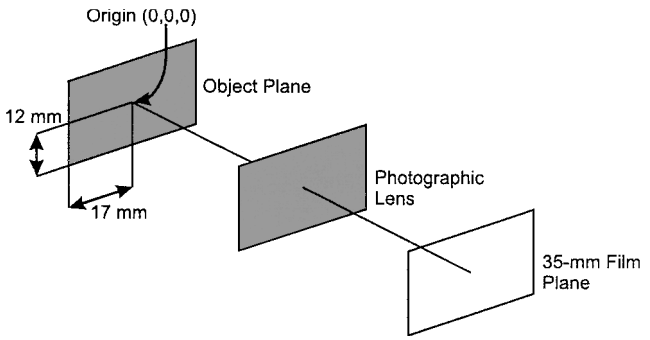

Fig. 4 Mapping of the object plane (left-hand side) to the image plane (right-hand side) under unity magnification; origin of the coordinate system is in the center of the object plane.

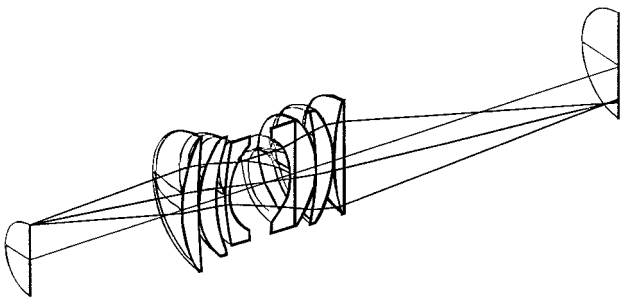

Fig. 5 Three-dimensional image of ray trace from a point object at location (0, 12, 0), through the compound 55-mm lens, and to the image plane.

During experiments, we typically use particles between 1 and 10 μm in diameter. At minimal aberration, the spot image from a 10-μm particle will be larger than the spot we predict using this point-source assumption. Our goal, however, is to explore the limits of aberration, in which case the actual size of the particle does not significantly alter our conclusions. Moreover, to propagate a distributed source via ray trace is extremely time consuming and uncertain.

Figure 6 shows more extensive imaging results in the form of spot diagrams. Figure 6 contains results for the 55-mm lens at f2.8, imaging 1:1. The center column, representing the z position for exact focus, contains three projected images for an object at 1) the origin (the upper image), 2) 12 mm from the origin (the center image, and 3) 17 mm from the origin (the bottom image). The four additional columns show spot diagrams for image planes separated by distances of ±0.100 and ±0.200 mm in the z direction. Note the appearance of astigmatism and coma for off-axis spots. Also note that the on-axis spots are sometimes smaller at values of z that are different from zero. This is because the code automatically finds a chromatic focus, wherein the average spot size for several colors is minimized. A single color may then focus at a slightly different value of z. In a subsequent case, for example, the spot at $\Delta z = -0.2$ is the smallest [at $\Delta z = -0.4$ (not shown) the spot grows again].

Changing lenses in the Sigma 2100 software is achieved by adjusting the parameters that describe a lens. As one example, the speed of the 55-mm lens was changed from f2.8 to f32 by changing the aperture, and a spot diagram was generated (Fig. 7). As another example, the optical prescription was changed from the 55-mm design to the 100 mm design (1:1 imaging again), and another spot diagram was produced at f32 (Fig. 8). Finally, the zoom lens was loaded and imaged at 10:1 (magnification = 0.1). An example spot diagram for it, at f8 is shown in Fig. 9.

Note, again, that the spot size investigation performed using ray-trace software neglects diffraction. The output of the ray-trace code, therefore, can include spot sizes smaller than the diffraction limit. Actual particle images will be a convolution of the Airy function with the geometric spot size at each lens speed.

Several conclusions may be drawn by comparing the spot diagrams in Figs. 6–9. (Note that they all use different length scales,

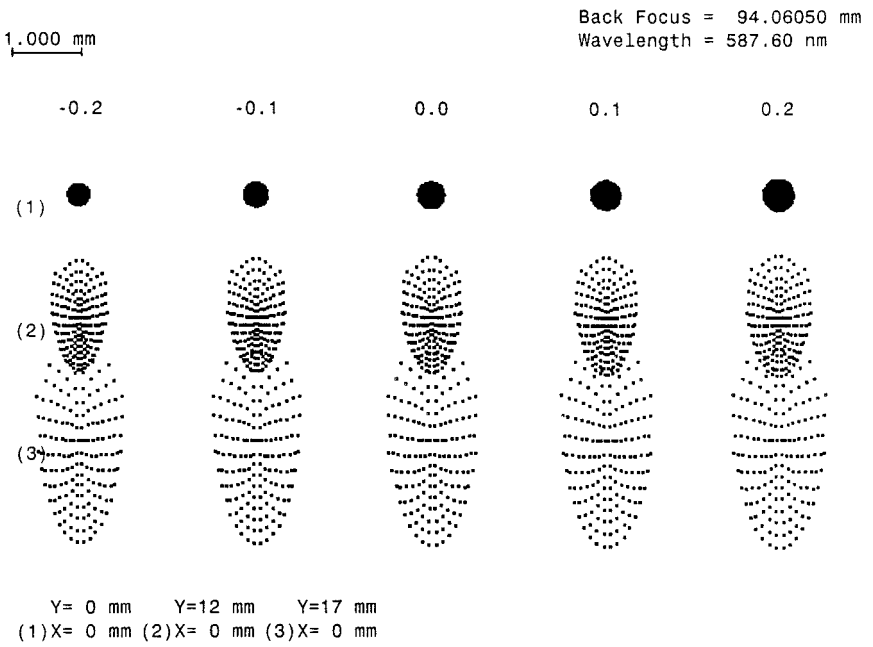

Fig. 6 Spot diagram for 55-mm lens at f2.8.

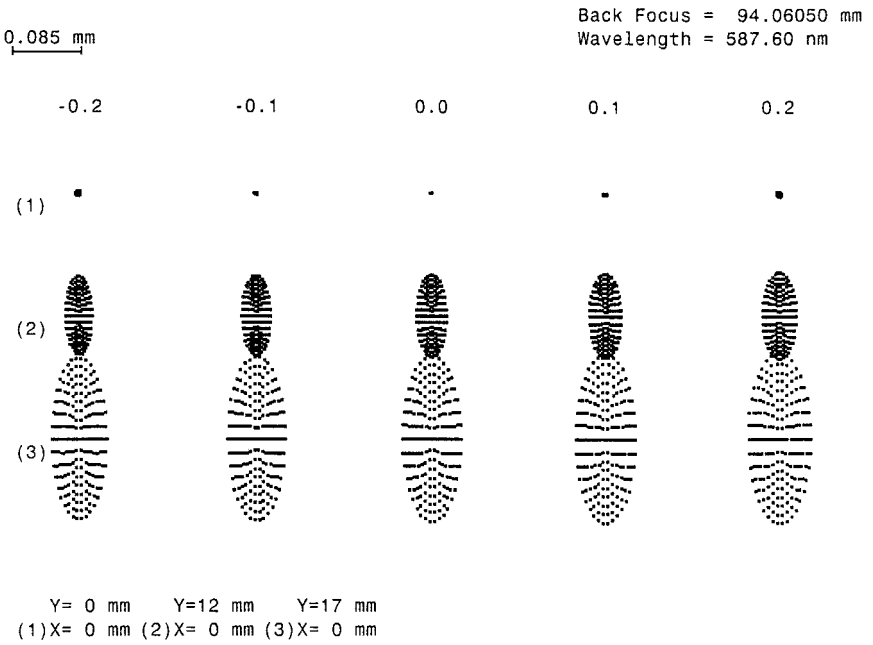

Fig. 7 Spot diagram (similar to Fig. 6) for 55-mm lens at f32 (length dimensions have changed); note the marked improvement in the on-axis spot size. On-axis aberrations are spherical, and a smaller aperture can improve them (more nearly paraxial behavior).

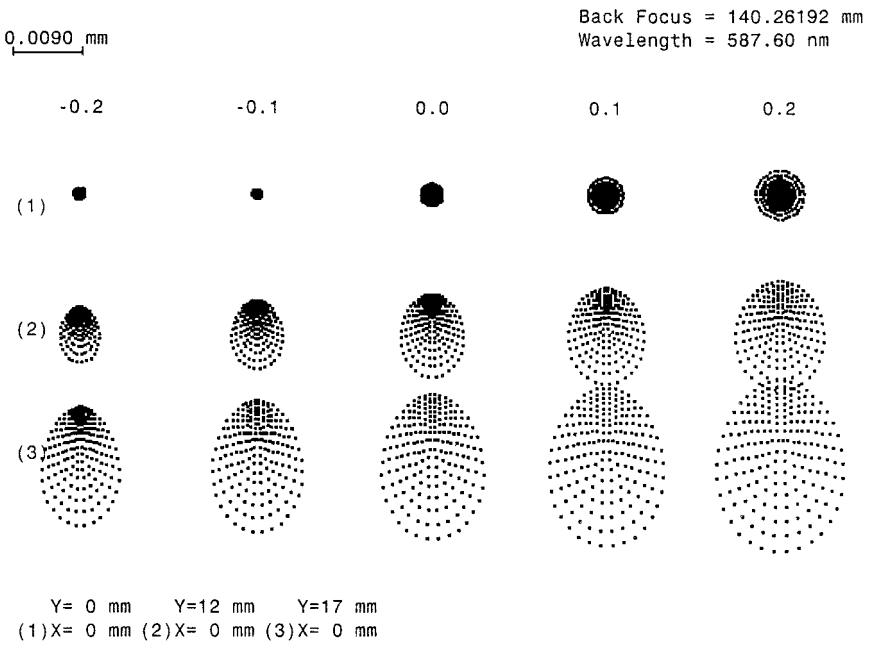

Fig. 8 Spot diagram (similar to Fig. 6) for 100-mm lens at f32. (Length dimensions have changed.)

shown in the upper-left-handcorner.) First, design compromises between curvature, glass, and lateral distance for each optical element of the respective photographic lenses are what produce the differences in ray distribution. Second, longer focal length lenses must use larger apertures to reach the same f-number as a smaller focal length lens. At the same f-number, therefore, a shorter focal length lens images in a more nearly paraxial configuration (relative the actual object and image distributions). Aberrations in the paraxial (on-axis) image are primarily spherical, and smaller apertures reduce spherical aberration. Counterbalancing this is that faster (shorter focal length lenses) usually require higher radii of curvature, exacerbating spherical aberrations (the rays are then less paraxial relative to the radius of curvature). Last, larger spot sizes occur as the object position migrates sideways, due to increasing aberration (primarily coma).

Next, image spot-size data were generated as a function of lens speed for all three lenses. In this portion of the study, a spot was located 12 mm from the center of the object plane and its image diameter measured at various lens speeds ranging from $f = 2.8$–32 (imaging 1:1 for the 55- and 100-mm lenses and imaging 10:1 for the zoom). These ray-trace results are plotted vs lens speed (f-number) in Figs. 10–12. Equation (4) is plotted for each lens as well, to demonstrate the contribution of diffraction to spot size. Adrian's[7] and Keane and Adrian's[8] imaging figure [Eq. (5)] is plotted as well, for comparison. Note that the change in magnification affects that curve in Fig. 12. A fourth curve represents an approximate convolution of the ray trace and diffraction spots. The ray-trace spots are fairly complex; to perform an accurate convolution would be quite difficult. In the spot size diagrams presented in Figs. 10–12, we simply added the diffraction spot size to the ray-trace spot size. Those curves are labeled estimated lens performance. In the regimes where the two sizes are quite different, the error introduced by this rough approximation is small (1–5%). In the regime where the spots are

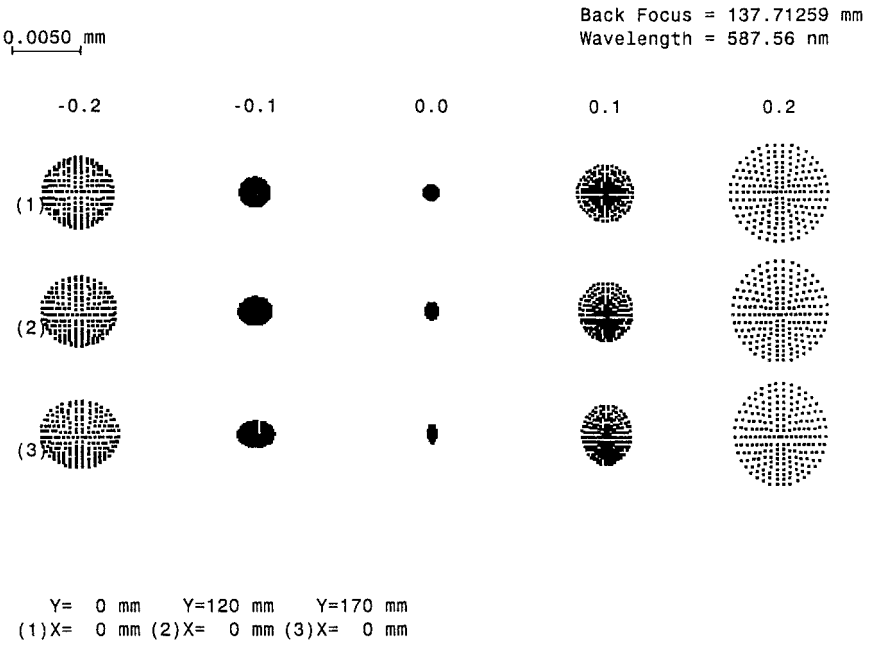

Fig. 9 Spot diagram (similar to Fig. 6) for zoom lens at f8 (length dimensions have changed); note the importance of spherical aberrations now that magnification is 0.1.

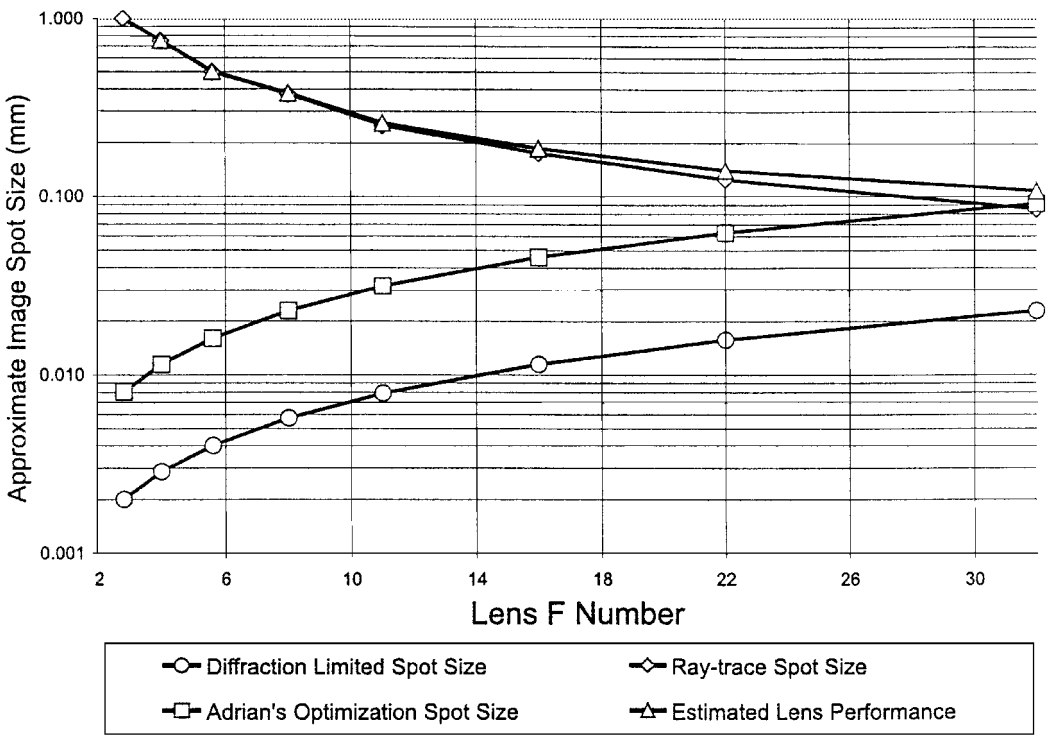

Fig. 10 Particle image spot size vs lens f-number for the 55-mm lens, 1:1 imaging; images are for spots originating at (0, 12, 0) in the object plane.

nearly equal in size, the error grows to 30%. Whereas this is a fairly large error, it occurs at f-numbers well outside the range we plan to discuss.

Several observations can be made regarding Figs. 10–12. First, of the 55- and 100-mm lenses, the 100-mm lens provides superior performance. This is because the 55-mm lens elements use higher radii of curvature, which exacerbates problems with aberrations. Moreover, the 55-mm lens is a much older design. Advancements in optical design tools have significantly improved the performance of modern lenses. The estimated lens performance curves in Figs. 10–12 show that aberration is the dominant source of distortion for lower f-numbers. As f-numbers are increased, that is, as the aperture is made smaller, optical aberrations are minimized and diffraction effects dominate. Note that the zoom data look fairly good. This is because the solid angle subtended by the lens is smaller, the object irradiance appears to be more collimated, that is, more nearly paraxial. Lens radii are also much longer, reducing spherical aberrations. There are tradeoffs to this lens, however. The small solid angle produces smaller signal strength at the film plane, and a zoom lens with magnification 10 has a very short depth of field. This point is obvious in Fig. 9 because the spot quickly grows with Δz. If the laser sheets are not matched to this short depth of field, then particles that fall outside the depth of field will be imaged with significant defocus. That problem could dominate any conclusion

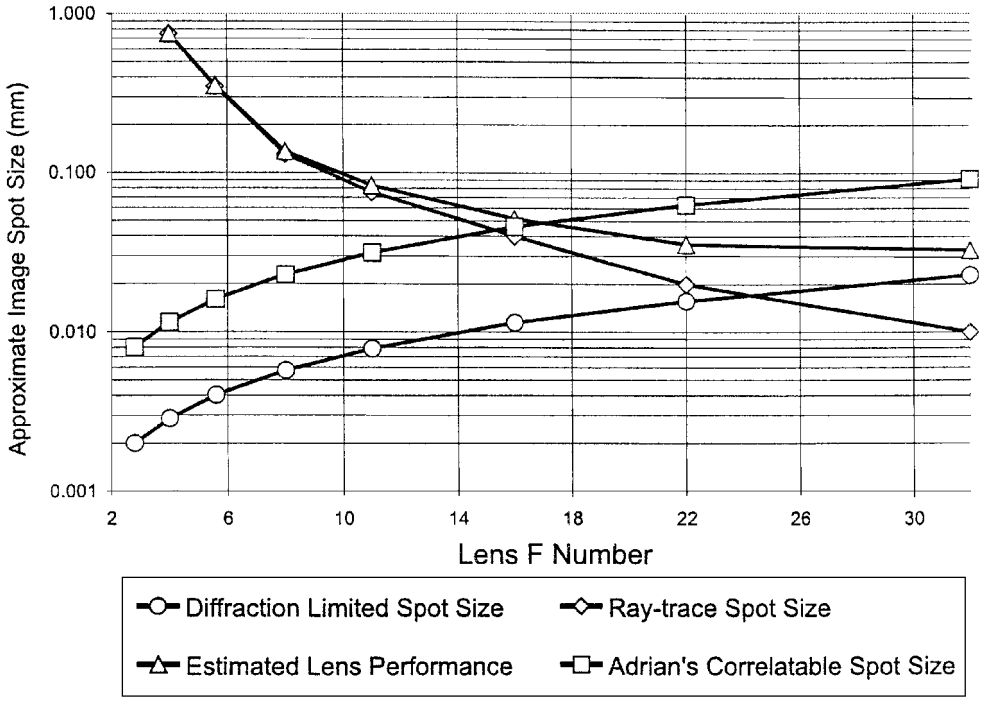

Fig. 11 Particle image spot size vs lens f-number for the 100-mm lens, 1:1 imaging; images are for spots originating at (0, 12, 0) in the object plane.

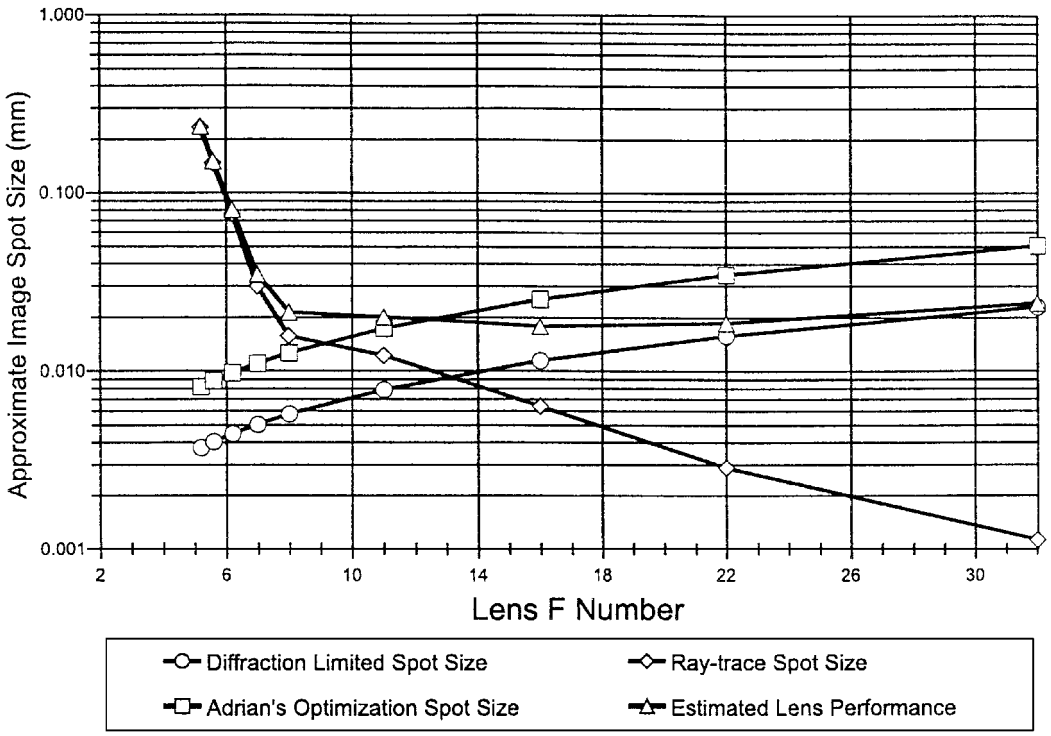

Fig. 12 Particle image spot size vs lens f-number for the zoom lens, 10:1 imaging; images are for spots originating at (0, 12, 0) in the object plane.

we draw here about particles that fall within the depth of field. This problem is also manifested in high sensitivity to misalignment, as we will show.

Based on our tolerance discussion in the subsection "Correlation Width and Particle Image Size," a conservative rule would be to hold the predicted spot sizes shown in the figures to below 30 μm. We believe that a fixed spot size criterion (such as this upper limit of 30 μm for any f-number) is the most useful tolerance. The ability of a software package to correlate images is not directly dependent on f-number, it is dependent on actual particle image size. Figures 11 and 12 indicate that we could achieve 30 μm spots at f18 and above for the 100-mm lens and at f8 and above for the zoom lens.

This may seem to contradict the common experience that it is usually possible to correlate images taken at f11 with a 100-mm lens, for example. The truth is that images can be correlated at f11 for a modern 100-mm lens. Unless exact alignment is achieved in the experiment, however, the image will have more off-axis dropouts and invalidated vectors than at f18. It is also true that images that do not meet our Whittaker-based tolerance can still be correlated; there is simply an increased error in the subpixel location of the peak. The spot size criterion is based on minimum absolute error in the subpixel peak location. This, too, can be relaxed somewhat. Our results, therefore, should be used simply for guidance, not as a hard rule. For example, aberrations climb rapidly in size for

ƒ-numbers less than 6, and, therefore, we do not recommend settings smaller than 6. We do not recommend using ƒ-numbers larger than what works well (ƒ8–ƒ18, for example) because that will simply reduce the light level collected at the image plane. Low light levels produce poor signal-to-noise ratios, making desired particle offset correlation peaks indistinguishable from noise correlation peaks.

Camera Defocus and Tilt

A more compelling reason for this study is the variation in focus and magnification one can encounter in an experimental setup. Clearly, camera defocus Δz is one source of this problem. Another cause of this problem is an insufficient depth of field. This occurs when the light sheet thickness is significantly larger than the depth of field as determined by the lens speed. Illuminated particles are then imaged with a large blur spot. Much of this has already been discussed by Adrian[7] and Keane and Adrian,[8] but we have applied the results of ray-trace analysis to extend that work.

A related problem is the effect of an excessive oblique camera-viewing angle (α; Fig. 13). In an ideal PIV configuration, the film plane and light sheet are completely parallel. In reality, they are at an angle α, which is often unknown.

To address these problems, we have performed ray-trace calculations to determine tolerances on defocus and tilt. In this work, we investigate the spot occurring at 12 mm off axis in the object plane. We then allow the camera to defocus or tilt to various angles and record the spot size. If it is possible to find a spot size (from a point off axis 12 mm in the object plane) that is smaller than 30 μm, we allow the camera to misalign until 30 μm is reached. If it is not possible to reach 30 μm, we simply give one example result. This defocus and tilt tolerance exercise was conducted for various camera ƒ-numbers.

Table 1 outlines the maximum allowable defocus and angular tolerance as a function of lens speed, for 100-mm lens. We chose not to analyze the 55-mm lens because it does not represent modern lens design. In Table 1, the values for Δz and α are those that will produce the spot size shown. When we state that a particular setting will probably correlate successfully, we are speaking from experience. The setting will most likely produce validated vectors, but we do not necessarily expect to meet the 30-μm criterion with that setting. Table 2 contains the same kind of information for the zoom lens.

Table 1 Allowable defocus and camera tilt for 100-mm lens

ƒ-number	α, deg	Δz, mm	δz, mm	Image diameter, mm	Successful correlation?
32	21.9	4.8	9.7	0.03	Yes
22	10.7	2.3	4.6	0.03	Yes
16	5.7	1.2	2.4	0.04	Probably
11	2.7	0.6	1.1	0.07	Probably
8	1.4	0.3	0.6	0.13	Possible
5.6	0.7	0.2	0.3	0.35	No

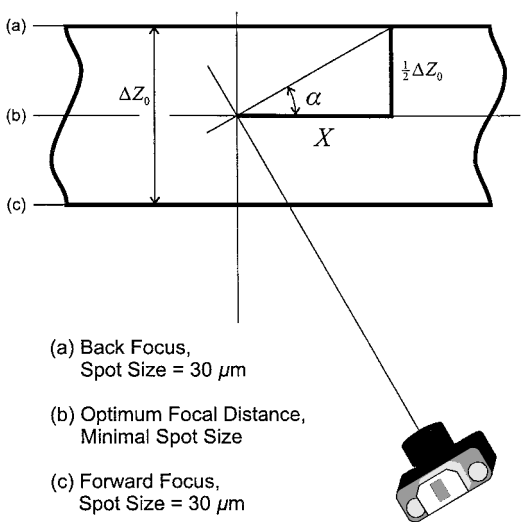

Fig. 13 Camera misalignment geometry.

Table 2 Allowable defocus and camera tilt for zoom lens

ƒ-number	α, deg	Δz, mm	δz, mm	Image diameter, mm	Successful correlation?
32	0.4	1.8	292	0.03	Yes
22	0.3	1.2	138	0.03	Yes
16	0.2	0.9	73	0.03	Yes
11	0.1	0.6	35	0.03	Yes
8	0.03	0.3	18	0.03	Possible

Note that successful correlation will ultimately depend on the nature of the flowfield, image interrogation technique, and the imaging optic employed. These results were intended for use in the design of an experiment alignment system, as described next.

Tables 1 and 2 also contain a diffraction-based depth of field, given by the formula

$$\delta z = 4(1 + M^{-1})^2(f)^2\lambda \tag{6}$$

where M is the magnification ($M = 1$ for 1:1, whereas $M = 0.1$ for 10:1). The ray-trace depth of field (in the object plane) is based on our Whittaker spot size tolerance. It is given by Δz for 1:1 imaging and by 10 Δz for 10:1 imaging. We present this information because the depth of field must be larger than the sheet thickness to bring illuminated particles into focus. Note that Eq. (6) overpredicts the depth of field roughly by 2 for 1:1 imaging and roughly by 10 for 10:1 imaging. This is an important outcome for design of a PIV experiment.

Uncertainty in Ray-Trace Results

There are two uncertainty issues here: uncertainty in the ray-trace code and the uncertainty arising from that the lens prescriptions used do not match existing lenses. With respect to the ray trace itself, the largest uncertainty arises in the optical prescription. There is a manufacturing uncertainty in the radii of curvature, the index of refraction for each glass element, and the spacing between lenses. A very simple parametric study indicates an uncertainty around ±5% in image spot size due to reasonable variations in lens design.

With respect to variation from manufacturer to manufacturer, we have several, chemical film-based experimental observations that corroborate the ray-trace results. On axis, measured particle images are on the order of 30 μm using a high-performance Nikon 100-mm lens at ƒ11. The data in Figs. 10–12 are for particles 12 mm off axis in the object plane, however, because we wish to explore the effect of aberrations on the full PIV field. We do measure larger off-axis images in acquired data using the 100-mm lens at ƒ11. There is some statistical variation among the measured image spots, but we do encounter some images as large as 80 μm (the size predicted by our ray-trace results). This result gives some measure of the uncertainty embedded in this kind of analysis; the ray-trace results are an upper limit, but the largest observed images are comparable to the ray-trace result. The ray-trace analysis is roughly within 30% of observations, based on images on chemical film. We did not perform a detailed comparison between film images and the ray-trace analysis, however, because there are always questions one can raise regarding the details of the experiment. The camera may not have been exactly at focus, it may have been tilted, the film may not have been developed properly, and so forth. The ray-trace results are less ambiguous and easier to manipulate to reach conclusions on camera usage (note that we do not own a zoom lens but we are able to analyze one in software).

For reasons given throughout (age of the available lens designs, comparison to our own results, etc.), we suggest that our ray-trace results be used as an upper limit on spot size. They offer information about trends in spot size, and they provide a conservative tolerance that would guarantee good correlation and peak detection errors.

Experiment Alignment System

The illumination sources used for PIV experiments at CSM consist of two Quanta-Ray GCR16 Nd:YAG lasers. For one-color PIV, the two frequency-doubled Nd:YAG lasers provide sequential green

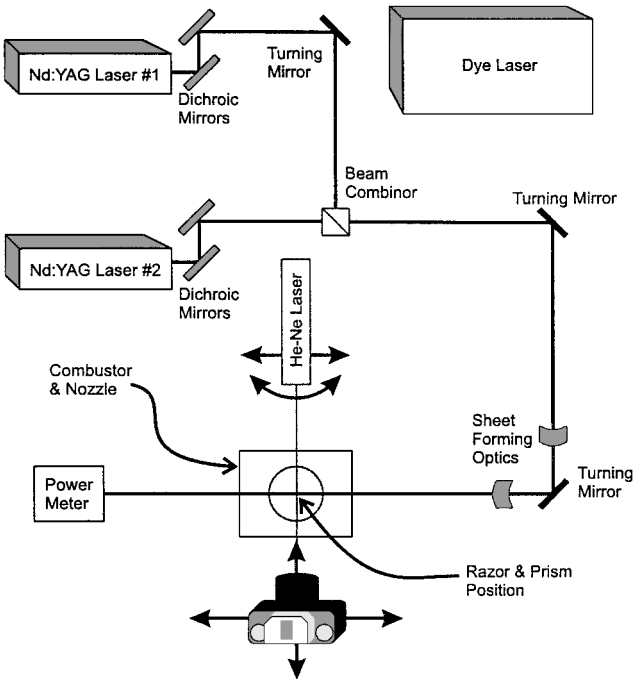

Fig. 14 Experimental setup.

illumination. For two-color PIV, output from one of the Nd:YAG lasers is used to pump a red dye laser (Quanta-Ray PDL-3). Whether two green pulses are used or one green and one red pulse are used, pulses are directed through a broadband polarizing optic that combines the two beams. The combined beam path is then directed through sheet forming optics and a test region by two additional mirrors. An optical-rail structure is constructed around the test region. It allows for adjustment of the optics while the center remains vacant for insertion of flowfields. A schematic of the experimental system appears in Fig. 14.

The optical alignment of components in a PIV experiment is the key to minimizing errors related to defocus and oblique angle. To compensate for cumulative effects on image distortion, a sequence of steps has been developed, emphasizing repeatability for successfully performing PIV. This alignment algorithm is described subsequently.

The standard approach using a digital camera is to align during experimentation. The PIV images appear in near-real time, and the system is optimized for best results. This is usually a valid approach. In the digital case, therefore, our tolerance exercise provides a guideline regarding what limits one should place on camera movement. As an example, if one can tilt the camera well beyond angular tolerances quoted in Tables 1 and 2, then the system may be acquiring images that produce larger peak location error than one may desire. One may be interested in controlling angle somewhat. The elaborate alignment approach we will describe was originally designed for chemical film PIV. It works well for digital PIV as well, but it is certainly not required. Once in place, however, realignments can be performed quickly. Although we do not perform PIV measurements in wind tunnels, it is our opinion that this technique can also be used to align such an experiment rapidly, no matter what kind of camera is used. In any case, portions of the technique can be adapted without using the entire procedure.

The first step in this new camera alignment algorithm is to ensure that the transverse optical paths of each pulse are matched and, thus, illuminate the same spatial sheet within the test region. To accomplish this task, a razor blade is scanned across the beam to measure each beam waist and location (the procedure is described by Wright et al.[11]). This is done before the waist, at the waist, and after the waist. Each laser is individually operated, and the beam alignment is adjusted until the beams are coincident. This procedure also provides a measurement of the sheet thickness. Typical measurements provide an average sheet thickness of 700 μm and offset between the two beams of $\leq$100 μm.

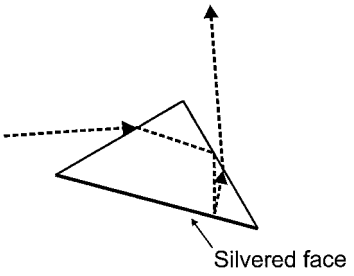

Fig. 15 Beam orthogonality using a silvered prism.

After beam overlap has been verified, the camera is positioned orthogonal to the light sheets using a helium–neon laser (HeNe) and roof prism. This alignment begins with placement of a precision right-angle roof prism at the point indicated in Fig. 14. The prism has a silvered, opaque hypotenuse, and it can ensure orthogonality between two beams to 0.036 deg. The operation of this prism is described by Taylor and Hafner.[12] It turns one beam through a right angle, as shows in Fig. 15. First, we transmit the aligned Nd:YAG beams (under very low energy) through several alignment diaphragm apertures, to the prism and onto the face of the HeNe, which is located as shown in Fig. 14. We then send the HeNe beam back through the prism, counterpropagating along the path taken by the Nd:Yag beams (Nd:YAG turned off in this step). Adjustments are then made in the HeNe laser position until the HeNe beam passes through diaphragm apertures. By tracing the HeNe beam that exits the prism back to one of these apertures, we measure an additional adjustment tolerance of $\pm$0.029 deg. Note that this is much less than the allowable values of α quoted in Table 1. It is close to the tolerance quoted in Table 2, but the zoom lens is for wind tunnel use. Such a setup would have much longer beam throws, and therefore, the ability to adjust angles would be significantly improved. The prism sets the ultimate tolerance, and it can still meet the required angles in Table 2. The camera film plane is then aligned by removing the prism and retroreflecting the HeNe from the camera and back onto itself. The gimbal mount for the camera offers sufficiently precise control to adjust the angle to within $\pm$0.03 deg. Therefore, we have good control of α.

Next, the camera is focused by continuously operating the YAG lasers and observing the images of flowfield particles in the image plane. Tables 1 and 2 indicate that one should have focusing resolution to hundreds of micrometers. Standard micrometer drives do, and so we set the camera at 1:1 imaging (in our case) and adjust the z position of the camera gimbal mount for best focus. The focus technique depends on the style of camera used. For a chemical film camera (Nikon F4 in our case) we do this by projecting the image collected by the lens onto a Nikon Type M focus screen located at the platform for the conventional single-lens reflex viewfinder. Registration for this precision focus screen is well within our tolerances. The screen has an etched cross hair, and so we mount a 50$\times$ microscope objective above the screen, focusing the objective on the cross hairs. The camera f-number is set to 2.8 (for rapid defocus while making adjustments). We then translate the camera in and out. We record the position at which images begin to go out of focus then reverse translation through focus and to the other extreme. We record that position as well, and then locate the camera halfway between the two positions. If the camera has been moved a long distance, it may be necessary to readjust the camera angle by retroreflection of the HeNe beam, but this is usually unnecessary. CCD systems can be similarly adjusted by watching the images on a monitor.

These steps consistently provide an optical alignment that is well within our tolerances.

Conclusions

In conclusion, by analyzing our correlation software, we have determined a particle image spot size for minimum error in subpixel peak location, for common configurations. Based on that finding, we have analyzed several camera lenses using a ray-trace code. This work has generated camera alignment tolerances for optimum PIV image acquisition. Using those tolerances, we have designed a system by which cameras can be quickly and accurately aligned to the experiment.

Acknowledgment

This work has been supported by the Center for Commercial Applications of Combustion in Space under NASA Cooperative Agreement NCCW-0096.

References

[1]Drouillard, T. F., II, "Mathematical Analysis of PIV Image Data, and Analysis of Implementation and Image Rendering on a PC," M.S. Thesis, Center for Commercial Applications of Combustion in Space, Colorado School of Mines, Golden, CO, Dec. 1998.

[2]McCarthy, P., "Successive Acquisition of Correlatable Images in Film-Based Particle Imaging Velocimetry," M.S. Thesis, Center for Commercial Applications of Combustion in Space, Colorado School of Mines, Golden, CO, Dec. 1998.

[3]Lourenco, L., and Krothapalli, A., "On the Accuracy of Velocity and Vorticity Measurements with PIV," *Experiments in Fluids*, Vol. 25, No. 6, 1995, pp. 421–428.

[4]Hecht, E., *Optics*, 3rd ed., Addison-Wesley, Reading, MA, 1998, pp. 461–465.

[5]Wolfram, S., *The Mathematica Book*, 3rd ed., Wolfram Media/Cambridge Univ. Press, Cambridge, England, U.K., 1996.

[6]Press, W. H., Teukolsky, S., A., Vetterling, W. T., and Flannery, B. P., *Numerical Recipes in C—The Art of Scientific Computing*, 2nd ed., Cambridge Univ. Press, Cambridge, England, U.K., 1992, pp. 412–425.

[7]Adrian, R., "Particle-Imaging Techniques for Experimental Fluid Mechanics," *Annual Review of Fluid Mechanics*, Vol. 23, 1991, pp. 261–304.

[8]Keane, R., and Adrian, R., "Optimization of Particle Image Velocimeters—Part 1: Double Pulsed Systems," *Measurement Science and Technology*, Vol. 1, No. 11, 1990, pp. 1202–1215.

[9]LensVIEW Database, Ver. Q4.03, Optical Data Solutions, Inc., New York, 1997.

[10]Bass, M. (ed.), *Handbook of Optics, Volume II, Devices, Measurements and Properties*, McGraw-Hill, New York, 1995, p. 16.3, Fig. 1.

[11]Wright, D., Greve, P., Fleischer, J., and Austin, L., "Laser Beam Width, Divergence, and Beam Propagation Factor—An International Standardization Approach," *Optical and Quantum Electronics*, Vol. 24, No. 9, 1992, S993.

[12]Taylor, S., and Hafner, E., "Turning a Perfect Corner," *American Journal of Physics*, Vol. 41, No. 1, 1979, pp. 113, 114.

J. P. Gore
Associate Editor